The Astrophysical Journal, 977:27 (15pp), 2024 December 10 https://doi.org/10.3847/1538-4357/ad79fa

Observations of Preferential Heating and Acceleration of α-particles in the Young Solar Wind by Parker Solar Probe

Jingyu Peng[1], Jiansen He[1], Die Duan[1], and Daniel Verscharen[2]
[1] School of Earth and Space Sciences, Peking University, Beijing 100871, Beijing, People's Republic of China; jshept@pku.edu.cn
[2] Mullard Space Science Laboratory, University College London, Dorking RH5 6NT, UK
Received 2023 December 4; revised 2024 August 17; accepted 2024 September 7; published 2024 November 29

Abstract

Remote sensing observations of the nascent solar wind in the solar corona imply that heavy ions are often faster and hotter than the plasma protons. In situ observations of the near-Earth solar wind with low collisional age show that hotter and faster states of heavy ions usually do not occur at the same time: heavy ions are either faster or hotter than the protons. This discrepancy highlights the need to understand the competing effects of heating, acceleration, Coulomb collisions, and instabilities on heavy ions in the inner heliosphere, from the solar corona to Earth. The Parker Solar Probe (PSP) is currently the closest spacecraft to the Sun and is anticipated to cross the outer boundary of the preferential heating and acceleration zone. Using in situ measurements from PSP, we find that larger drift speeds between α-particles and protons ($V_{\alpha p}$) correspond to larger α-to-proton temperature ratios ($\frac{T_\alpha}{T_p}$) in the young solar wind close to the corona. This observation differs from in situ observations farther from the Sun (e.g., with Helios and Wind at 0.3–1 au). We believe that this difference is related to the speed of the solar wind, as well as the distance from the Sun. The anti-correlation between $V_{\alpha p}$ and $\frac{T_\alpha}{T_p}$ in fast wind away from the Sun is potentially related to the energy transfer from the drift kinetic energy of α-particles to proton thermal energy due to drift instabilities. In the young slow wind, heavy ions exhibit signs of both preferential heating and preferential acceleration, but are not affected much by drift instabilities. We identify the outer boundary of the preferential heating and acceleration zone for heavy ions in the young slow wind to be at a distance of around 0.16 au, beyond which the effects of Coulomb collisions weaken the effects of preferential heating and acceleration.

Unified Astronomy Thesaurus concepts: Solar wind (1534)

1. Introduction

The plasma of the solar wind is heated to temperatures of order a million Kelvin in the corona and accelerated to speeds of hundreds of kilometers per second while escaping the Sun. The solar wind ion composition predominantly consists of protons, accounting for about 95% of the ion number density, and heavy ions including α-particles, which are the most abundant of the heavy ions, accounting for about 5% of the number density. The abundance of α-particles varies with the type of solar wind (D. E. Robbins et al. 1970; J. C. Kasper et al. 2007). Remote-sensing observations of the O^{5+} spectral line in the solar atmosphere using the Solar and Heliospheric Observatory/Ultraviolet Coronagraph Spectrometer (SOHO/UVCS) reveal that the O^{5+} effective temperature increases rapidly with the radial distance, with the effective temperature exceeding the proton temperature by a factor of up to 100 at distances of less than 1 $R_{\rm Sun}$ from the solar surface, where $R_{\rm Sun}$ is the solar radius (S. R. Cranmer 2009). Based on UVCS spectral observations, Doppler dimming inversion reveals that the flow velocity of O^{5+} increases rapidly in close proximity to the solar surface at a distance of 1 $R_{\rm Sun}$, exceeding the velocity of the proton flow. These observations suggest that preferential heating and preferential acceleration of heavy ions occur in the corona and extend into the inner heliosphere. Several theories have been proposed to explain this phenomenon, including resonant wave–particle interactions (S. R. Cranmer 2000; S. P. Gary et al. 2001; J. V. Hollweg & P. A. Isenberg 2002; S. P. Gary et al. 2005; J. C. Kasper et al. 2013), velocity filtration (J. D. Scudder 1992), stochastic heating (B. D. G. Chandran et al. 2010, 2013), intermittent current-dissipation heating in low-frequency Alfvénic turbulence (W. H. Matthaeus et al. 1999), and magnetic reconnection (P. J. Cargill & J. A. Klimchuk 2004; J. F. Drake et al. 2009). It is unclear which of these mechanisms is the dominant one in the preferential heating and acceleration of heavy ions.

Observations from the Wind spacecraft over more than two decades at a heliocentric distance of 1 au demonstrate that in weakly collisional solar wind, α-particles are about 5 times hotter than protons, with α-to-proton drift speeds parallel to the local magnetic field comparable to the local proton Alfvén speed, $V_{\rm A}\left(=\frac{B}{\sqrt{\mu_0 n_p m_p}}\right)$, where μ_0 is the magnetic permeability of free space, B is the magnetic flux density, m_p is the proton mass, and n_p is the proton number density (E. Marsch et al. 1982; P. J. Tracy et al. 2016; J. C. Kasper et al. 2017). Detailed investigations of the weakly collisional solar wind reveal that plasma with higher α-to-proton temperature ratios exhibits lower drift speeds (E. Marsch et al. 1982; L. Berger et al. 2011). Resonant heating by ion cyclotron waves (ICWs; J. C. Kasper et al. 2013) and the stochastic heating in low-frequency kinetic Alfvén turbulence (B. D. G. Chandran et al. 2013) predict this relationship between the temperature ratio and drift speed.

Observations by the Helios spacecraft provide information on the radial development of the α-particle drift speed and the α-to-proton temperature ratio in the solar wind from 0.29 to 0.8 au. The ratio of drift speed to the local Alfvén speed decreases as the heliocentric distance increases (E. Marsch et al. 1982; T. Ďurovcová et al. 2017). While both the proton and α-particle temperatures decrease

as a function of the radial distance, the parallel temperature of the α-particles decreases faster than the adiabatic prediction, which suggests the existence of a parallel cooling mechanism for α-particles. On the contrary, the perpendicular temperatures of both protons and α-particles decrease more slowly than the adiabatic prediction, suggesting the presence of perpendicular ion heating (D. Stansby et al. 2019). Constraints on the drift speed of α-particles relative to protons due to drift instabilities have been intensively investigated (e.g., S. P. Gary et al. 2000a, 2000b, 2003; Q. Lu et al. 2006; D. Verscharen et al. 2015; X. Zhu et al. 2023). The radial evolution of the drift speed is often constrained by the threshold of the fast magnetosonic/whistler (FM/W) instability (D. Verscharen et al. 2015). The energy release associated with this deceleration mechanism suggests that α-particles play an important role in the energetics of the solar wind within 1 au.

The Parker Solar Probe (PSP) has extended our in situ measurements of the solar wind to distances of less than 0.1 au from the Sun and thus closer to the region where the solar corona is heated. According to PSP observations, α-particles are faster than the protons in most cases. Furthermore, the α-to-proton drift speed decays almost completely before reaching the Helios orbit in the slow wind (P. Mostafavi et al. 2022). This explains the lack of observed α-to-proton velocity differences in the slow wind away from the Sun. In highly Alfvénic and spherically polarized switchbacks, α-particles and protons follow different circular arcs in the wave reference frame in velocity space (M. D. McManus et al. 2022). The velocity and magnetic field perturbations are either in-phase or anti-phase correlated.

Remote sensing observations by UVCS show that near the Sun, heavy ions are accelerated to higher speeds than protons and heated to higher temperatures than protons. However, observations from the Wind spacecraft suggest that the positive correlation between the α-to-proton temperature ratios and α-to-proton drift speeds does not survive to 1 au (J. C. Kasper et al. 2013). Observations from Helios show that the α-to-proton temperature ratio and drift speed change with distance from the Sun, indicating differences from the results at 1 au. This study aims to examine the distribution of the α-to-proton temperature ratios and drift speeds in the very inner heliosphere measured by PSP. Our goal is to combine observations from PSP and Helios spacecraft to understand the radial evolution of the correlation between the α-to-proton temperature ratios and drift speeds.

According to UVCS remote-sensing observations, the inner boundary of the preferential heating zone is just above the solar surface at an altitude of less than one solar radius (D. Telloni et al. 2007). However, the location of the outer boundary of the preferential heating zone, if it exists, is still unknown. An empirical model for the outer boundary of this zone combines interplanetary solar wind measurements with a temperature evolution model that accounts for Coulomb collisions (J. C. Kasper et al. 2017). Based on 20 yr of observations from Wind, the model suggests that the preferential heating zone extends from the transition region of the lower corona to an outer boundary approximately 20–40 solar radii from the Sun. The α-to-proton temperature ratio in the preferential heating zone is characterized by a super-mass-proportional ratio of $\sim$5. The preferential ion heating beyond the transition region indicates that this phenomenon is important for the evolution of the outer corona and the young solar wind. The outer boundary of the preferential heating zone is closer to the Sun than previous spacecraft (e.g., Wind, Helios, and Messenger) orbits, meaning that prior spacecraft only measured residual signals of preferential heating from outside the zone. The previous model predicts that PSP is likely to be the first spacecraft to approach the Sun close enough to penetrate the outer boundary of the preferential heating zone and directly observe its physical mechanisms (J. C. Kasper et al. 2017). Our study uses PSP observations to identify the outer boundaries of the preferential heating and acceleration zones.

In this study, we determine the nonthermal properties of heavy ions and protons and their differences as observed by PSP. We investigate to what degree these properties are consistent with the in situ measurements at larger radial distances by other spacecraft, and then whether PSP observes the outer boundaries of the preferential heating or acceleration zones.

We introduce the data used in this paper in Section 2. In Sections 3.1 and 3.2, we analyze the PSP and Helios data to demonstrate the nonthermal properties of the solar wind at different radial distances. In Section 3.4, we identify the outer boundaries of the preferential heating and acceleration zones. Discussions on the evolution of nonthermal properties of the solar wind during its propagation form Section 4.

2. Observations

We use data from PSP's 6th to 10th encounters between 2020 August and 2022 January. During this period, PSP reached a minimum distance from the Sun of about 0.0618 au (about $13R_{\rm Sun}$). We adopt data from the PSP/SWEAP/SPAN-ion instrument for plasma measurements (R. Livi et al. 2022) and data from the PSP/FIELDS instrument for magnetic field measurements (S. D. Bale et al. 2016). The plasma data include protons and α-particle number densities, velocity vectors, as well as parallel and perpendicular temperatures. The PSP data vary in time resolution according to the detection mode (encounter-phase and cruise-phase measurements). The sampling rate of the magnetic field is 2.3 samples s^{-1} for the cruise phase. For the encounter phase, the maximum sampling rate is 293 samples s^{-1} (T. A. Bowen et al. 2020). The time resolution for the most commonly used plasma data modes is either 7 s or 3.5 s. Of all the data we use, the α-particle data exhibit the lowest temporal resolution. For the sake of our subsequent analysis, we take the time point of the α-particle data as the reference time point, and interpolate the proton and magnetic field data to the reference time point. For comparative analysis, we also use Helios plasma and magnetic field data from 1975 to 1977 (D. Stansby et al. 2019), which range in heliocentric distance from 0.29 to 0.78 au and have a time resolution of 40 s. We define the field-aligned drift speed $V_{\alpha p}$ as the projection of the difference in flow velocity between α-particles and protons in the direction of the magnetic field $\boldsymbol{B}$, calculated as $V_{\alpha p} = (\boldsymbol{V}_\alpha - \boldsymbol{V}_p) \cdot \frac{\boldsymbol{B}}{|\boldsymbol{B}|}$, where $\boldsymbol{V}_\alpha$ and $\boldsymbol{V}_p$ are the bulk velocities of α-particles and protons, respectively.

3. Analysis and Results

3.1. Radial Evolution of Solar Wind Protons and α-particles

Figure 1 displays the radial evolution of number density n, radial velocity V_r, perpendicular temperature $T_\perp$, parallel temperature $T_\parallel$, and temperature anisotropy (characterized by $A = \frac{T_\perp - T_\parallel}{T_\perp + T_\parallel}$) for both α-particles and protons in the heliocentric distance range of 0.06–0.4 au. The distribution of the radial

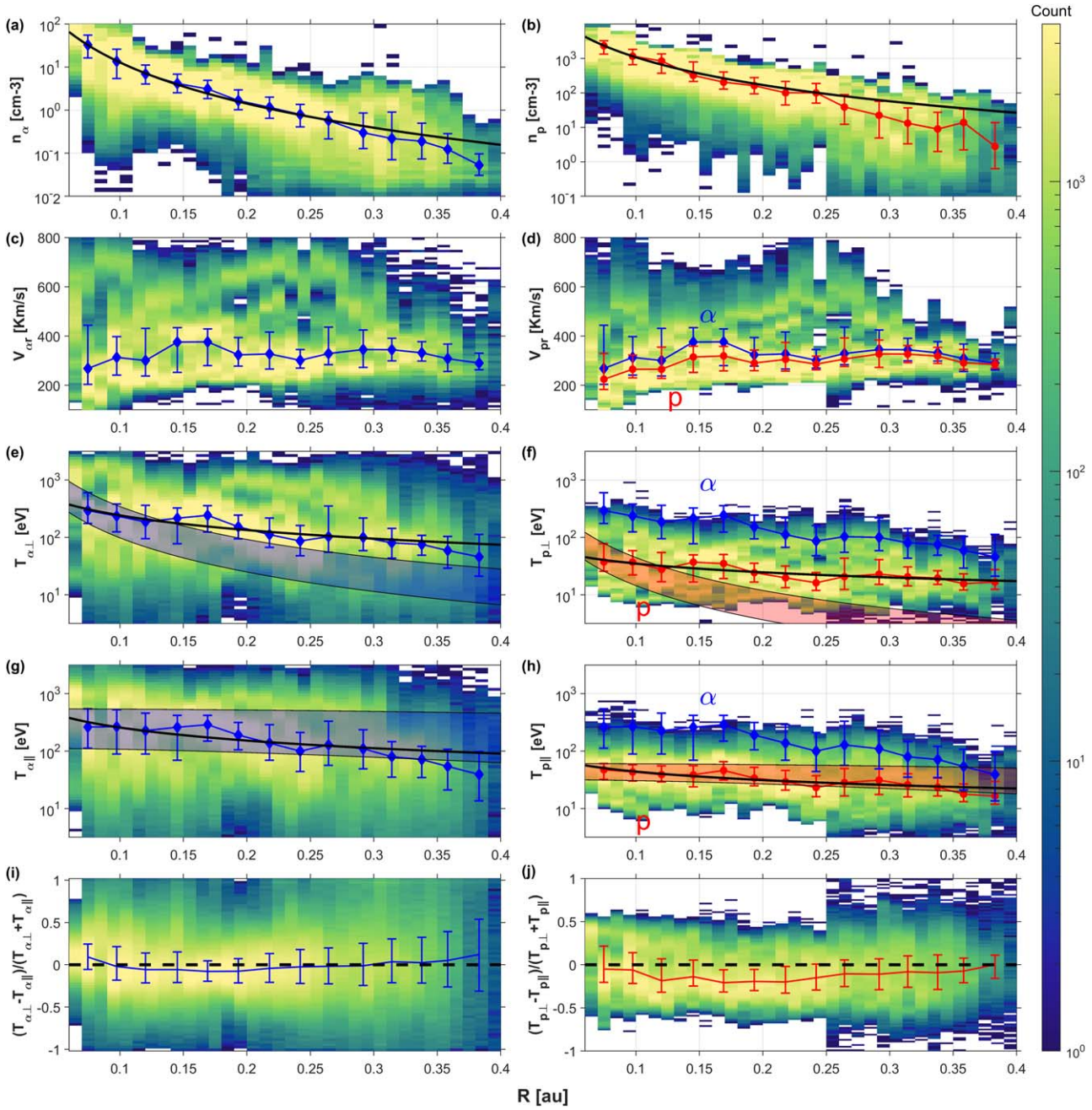

Figure 1. Radial evolution of the number density n, radial velocity V_r, perpendicular temperature $T_\perp$, parallel temperature $T_\parallel$, and temperature anisotropy $\frac{T_\perp - T_\parallel}{T_\perp + T_\parallel}$ for α-particles (left panels) and protons (right panels). The color bars on the right indicate the number of counts in each bin. The blue and red curves represent the local median value of the parameters for α-particles and protons, with the error bars indicating the quartiles of the local distributions. In panels (a), (b), (e), (f), (g), and (h), the median values are fitted with a power-law function and the result is depicted as black solid curves. The shaded regions in panels (e), (f), (g), and (h) display the model prediction using the double adiabatic theory to predict the radial evolution of perpendicular and parallel temperatures, assuming a proton flow speed in the range of 200–400 km s^{-1}. For reference, temperature isotropy is indicated by the black dashed lines in panels (i) and (j).

velocity with respect to heliocentric distance (Figures 1(c) and (d)) exhibits a baseline for the lower limit of radial changes in the flow speed, revealing a minimum solar wind speed, which we refer to as the "calm background" solar wind. We speculate that the "calm background" solar wind experiences minimal heating and acceleration due to waves/turbulence or reconnection, in contrast to the faster and more turbulent solar wind. From the radial profile of the velocity distribution median value, we find a radial acceleration within 0.15 au for both α-particles and protons. α-particles exhibit higher perpendicular and parallel temperatures compared to protons (as shown in Figures 1(f) and (h)). Furthermore, the average temperature ratios of α-particles to protons are remarkably greater than the mass ratio in both the perpendicular and parallel directions, with $\frac{T_\alpha}{T_p} \sim 6.3 (>4)$. The temperature difference between α-particles and protons gradually diminishes with increasing heliocentric distance beyond 0.15 au (see Figures 1(f), (h) and 2(a)).

For 0.06 au $\leq r \leq$ 0.4 au, we fit a power function to the radial trends of the number density and temperature (indicated

by the black curves in Figures 1(a), (b), (e), and (h)):

$$n_\alpha(r) = 0.00847\ \mathrm{cm}^{-3}\left(\frac{r}{1\ \mathrm{au}}\right)^{-3.2}, \quad (1)$$

$$n_p(r) = 2.27\ \mathrm{cm}^{-3}\left(\frac{r}{1\ \mathrm{au}}\right)^{-2.68}, \quad (2)$$

$$T_{\alpha\perp}(r) = 34.1\ \mathrm{eV}\left(\frac{r}{1\ \mathrm{au}}\right)^{-0.850}, \quad (3)$$

$$T_{\alpha\parallel}(r) = 45.3\ \mathrm{eV}\left(\frac{r}{1\ \mathrm{au}}\right)^{-0.754}, \quad (4)$$

$$T_{\alpha}(r) = 41.1\ \mathrm{eV}\left(\frac{r}{1\ \mathrm{au}}\right)^{-0.788}, \quad (5)$$

$$T_{p\perp}(r) = 10.9\ \mathrm{eV}\left(\frac{r}{1\ \mathrm{au}}\right)^{-0.509}, \quad (6)$$

$$T_{p\parallel}(r) = 14.1\ \mathrm{eV}\left(\frac{r}{1\ \mathrm{au}}\right)^{-0.493}, \quad (7)$$

$$T_{p}(r) = 11.8\ \mathrm{eV}\left(\frac{r}{1\ \mathrm{au}}\right)^{-0.533}. \quad (8)$$

Both the α-particle and proton densities decay faster than the inverse square with the radial distance. This behavior suggests a radial increase in the flow velocity of the two-particle species within 0.15 au, assuming a constant flux of particles. In addition, we observe a faster radial decay of the α-particle density and temperature compared to that of the protons in the investigated heliocentric distance range. This indicates that the radial evolutions of the proton and α-particle velocities exhibits different behaviors, which in turn result in different radial evolutions of the densities. The phenomenon of faster temperature decay for α-particles (whose temperatures tend to approach the temperature of protons) occurs mostly beyond 0.15 au and may be attributed to a rebalancing of the preferential heating between protons and α-particles with distance and the increasing relative importance of energy exchange between α-particles and protons due to Coulomb collisions and wave–particle interactions.

Without Coulomb collisions or wave–particle interactions, the plasma's thermal variation is expected to conform with the double adiabatic law (G. F. Chew et al. 1956). Previous studies (L. Matteini et al. 2012; D. Stansby et al. 2019) use the double adiabatic law to evaluate the radial trends of solar wind temperature variations and to compare them to observations. Similarly, variations of perpendicular and parallel temperatures of protons and α-particles as functions of the radial distance are also estimated in this study between 0.06 and 0.4 au. According to the double adiabatic prediction, the perpendicular and parallel temperatures are related to the magnetic field and number density, which are expressed using the following equations:

$$T_{\perp 2} = T_{\perp 1}\frac{|B_2|}{|B_1|}, \quad (9)$$

$$T_{\parallel 2} = T_{\parallel 1}\left(\frac{n_2}{n_1}\frac{|B_1|}{|B_2|}\right)^2, \quad (10)$$

where subscripts 1 and 2 represent the variables at two radial distances.

Figures 1(e)–(h) display the trends in perpendicular and parallel temperatures of protons and α-particles, as predicted by the double adiabatic theory, with the reference temperature being the temperature at 0.07 au. To simplify, we use the Parker interplanetary magnetic field model (E. N. Parker 1958), and the number density follows a quadratic decrease with radial distance. Comparing these predictions with PSP observations reveals that the radial decrease in the perpendicular temperature of both α-particles and protons is slower than the predicted trend from the double adiabatic theory. This slower decrease in the perpendicular temperature is consistent with previous observations made by Helios between 0.29 and 0.8 au (D. Stansby et al. 2019). On the other hand, the radial trend of the parallel temperature for both α-particles and protons agrees well with the predicted trend from the double adiabatic theory, indicating that the solar wind in both PSP and Helios observations undergoes sustained heating preferentially in the perpendicular direction.

Various ion heating theories predict the occurrence of perpendicular heating, resulting in thermal anisotropy where the perpendicular temperature is greater than the parallel temperature. Examples of such theories include ion cyclotron resonance heating by ICWs (J. C. Kasper et al. 2013), stochastic ion heating by kinetic Alfvén wave turbulence (B. D. G. Chandran et al. 2013), as well as the displacement and perpendicular energization effects from turbulent electromagnetic fields in magnetohydrodynamic turbulence (F. Pugliese & P. Dmitruk 2022). Nonetheless, PSP does not observe significant thermal anisotropy in the perpendicular temperature of α-particles, as demonstrated in Figure 1(i) with $\frac{T_{\alpha\perp}-T_{\alpha\parallel}}{T_{\alpha\perp}+T_{\alpha\parallel}} \sim 0$, in the inner heliosphere. In a similar vein, the mean anisotropy of the proton temperature is insignificant at approximately 0.1 au and 0.4 au. At 0.2 au, the parallel temperature is higher, leading to a valley in the curve for $\frac{T_{p\perp}-T_{p\parallel}}{T_{p\perp}+T_{p\parallel}}$ in Figure 1(j). This observation suggests that parallel heating mechanisms other than those mentioned earlier are responsible for the large parallel temperatures. For instance, the forward cascade and dissipation heating of decaying kinetic Alfvénic turbulence may increase the parallel temperature of ions (T. N. Parashar & S. P. Gary 2019). The results of their 2.5-dimensional particle-in-cell simulations reveal that the thermal anisotropy of ions changes monotonically with time, with the ratio of parallel to perpendicular temperature increasing. This indicates that more energy is transferred from turbulent energy to parallel thermal energy rather than to perpendicular thermal energy in these simulations.

3.2. Radial Evolution of Nonthermal Properties of Solar Wind Protons and α-particles

Figure 2 illustrates the evolution of nonthermal properties of protons and α-particles, including the α-to-proton temperature ratio $\frac{T_\alpha}{T_p}$, normalized α-to-proton drift speed $\frac{V_{\alpha p}}{V_A}$, and temperature anisotropy (characterized by $\frac{T_\perp}{T_\parallel}$), as functions of the radial distance (left panel), and as functions of the Coulomb collision number N_C, which counts the number of Coulomb collisions that a solar wind particle would experience as it propagates to the spacecraft location:

$$N_C = \int_{r_0}^{r} \nu_{\alpha p}(s)\frac{ds}{u(s)}, \quad (11)$$

where $\nu_{\alpha p}$ is the Coulomb collision frequency between α-particles and protons, and u is the solar wind bulk speed. The initial radial position r_0 is set to 2.5 solar radii, the approximate source surface position (J. T. Hoeksema et al. 1983). The final

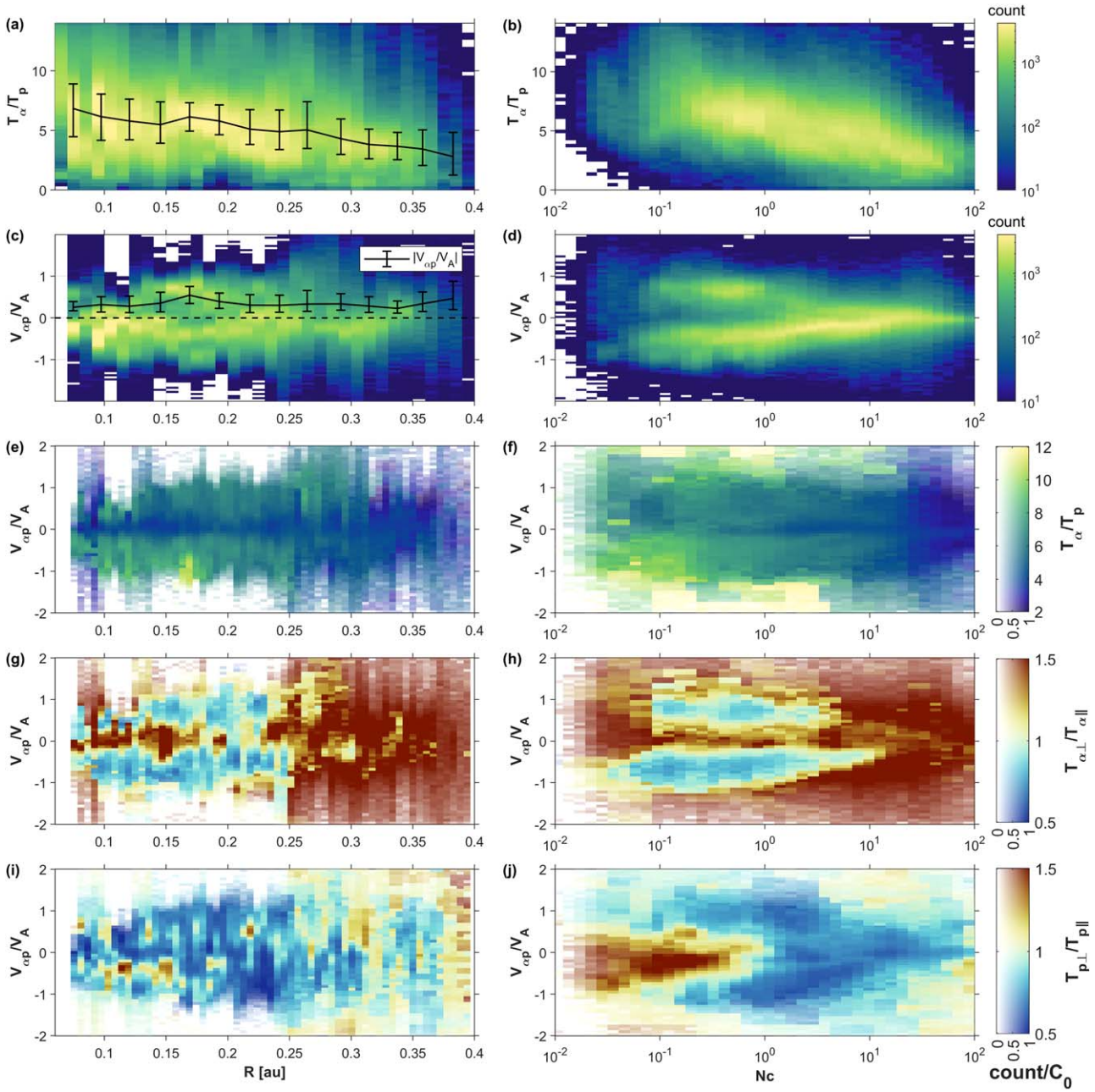

Figure 2. Variations in the α-to-proton temperature ratios and drift speeds as functions of the radial distance (left column) and Coulomb collision number (right column). Panels (a)–(d) show the count distribution in each bin. Panels (e) and (f) display the average temperature ratio $\frac{T_\alpha}{T_p}$, with its average value indicated by the color bar. Panels (g) and (h) depict the average α-particle temperature anisotropy $\frac{T_{\alpha\perp}}{T_{\alpha\parallel}}$, while panels (i) and (j) show the average proton temperature anisotropy $\frac{T_{p\perp}}{T_{p\parallel}}$. The color saturation of the bins in panels (e)–(j) is determined by the number of counts in each bin, with a threshold set at $C_0 = 100$. In panels (a) and (c), the black solid curves represent the median of $\frac{T_\alpha}{T_p}$ and $\left|\frac{V_{\alpha p}}{V_A}\right|$ within the segmented heliocentric distance range, and the error bars represent the local first and third quartiles. The black dashed line in panel (c) marks the position of zero drift speed.

radial position r is the spacecraft's position. The calculation of N_C is given in the Appendix.

The ratio $\frac{T_\alpha}{T_p}$ shows a decreasing trend with the radial distance. The median value drops from approximately 6 near 0.1 au to approximately 4 near 0.35 au, as shown in Figure 2(a). As shown in Figure 2(c), the average $\frac{V_{\alpha p}}{V_A}$ rises initially up to 0.15 au and then declines as the radial distance increases. On average, the solar wind drift speed between protons and α-particles is smaller than V_A at all radial distances. From Figure 2(e), $\frac{T_\alpha}{T_p}$ is lower when the drift speed is low ($\frac{V_{\alpha p}}{V_A} \sim 0$), but becomes higher (e.g., $\frac{T_\alpha}{T_p} > 6$) as the drift speed increases ($\frac{V_{\alpha p}}{V_A} > 0$). This suggests that preferential heating is insignificant when the drift speed is low, but becomes more prominent as the drift speed increases. This outcome contrasts with the Wind observations at 1 au where the α-particle temperature is greater at low drift speed and less notable at high drift speed (J. C. Kasper et al. 2013). The drift speed is often considered a key parameter characterizing the preferential acceleration of heavy ions. According to the PSP observations,

preferential acceleration and preferential heating of solar wind heavy ions coexist in the inner heliosphere, at least within 0.06–0.4 au from the Sun.

Figures 2(b) and (d) show that $\frac{T_\alpha}{T_p}$ and $\frac{V_{\alpha p}}{V_A}$ decrease as N_C increases, suggesting that Coulomb collisions significantly reduce the nonthermal properties of the solar wind. Similar occurrences have also been documented at 1 au. This is believed to be a result of the gradual decrease of nonthermal properties caused by Coulomb collisions as the solar wind expands (J. C. Kasper et al. 2008; P. J. Tracy et al. 2016; J. C. Kasper et al. 2017; E. Johnson et al. 2023). In Figure 2(f), the high $\frac{T_\alpha}{T_p}$ appears at small N_C ($10^{-2}-1$) and high $\frac{V_{\alpha p}}{V_A}$. When N_C becomes larger, the high $\frac{T_\alpha}{T_p}$ considerably diminishes, which indicates that Coulomb collisions reduce the temperature ratio.

We plot the evolution of α-particle temperature anisotropy and proton temperature anisotropy with the radial distance and N_C in Figures 2(g)–(j). α-particles at $R<0.25$ au exhibit on average $\frac{T_{\alpha\perp}}{T_{\alpha\parallel}}>1$ when $\frac{V_{\alpha p}}{V_A}\sim 0$ and $\frac{T_{\alpha\perp}}{T_{\alpha\parallel}}\leqslant 1$ when $\frac{V_{\alpha p}}{V_A}>0$. For $R>0.25$ au, the average $\frac{T_{\alpha\perp}}{T_{\alpha\parallel}}>2.5$ is largely independent of the drift speed. The proton temperature anisotropy does not have a clear correlation with the radial distance but is considerably dependent on N_C. At smaller N_C, $\frac{T_{p\perp}}{T_{p\parallel}}$ can be as high as 1.4. With increasing N_C, the parallel temperature of protons becomes higher than the perpendicular temperature, leading to $\frac{T_{p\perp}}{T_{p\parallel}}$ smaller than 1. The shift occurs first at locations with larger $\frac{V_{\alpha p}}{V_A}$.

Figure 3 combines in situ data from the PSP and Helios spacecraft and illustrates the distributions of $\beta_{p\parallel}=\frac{n_p k_B T_{p\parallel}}{|\vec{B}|^2/2\mu_0}$, normalized drift speed $\frac{V_{\alpha p}}{V_A}$, α-to-proton temperature ratio $\frac{T_\alpha}{T_p}$, and ion thermal anisotropy $\frac{T_\perp}{T_\parallel}$, at various radial distances. Here k_B is the Boltzmann constant. The top row presents the results for PSP within 0.4 au, the middle row presents the results for Helios within 0.29–0.5 au, and the bottom row presents the results for Helios beyond 0.5 au. As demonstrated in Figure 3(b), a greater $\frac{V_{\alpha p}}{V_A}$, as observed by PSP, correlates with an increased $\frac{T_\alpha}{T_p}$. For small $\frac{V_{\alpha p}}{V_A}$, $\frac{T_\alpha}{T_p}$ is also lower, which is consistent with the observations shown in Figure 2(e). The positive correlation between $\frac{T_\alpha}{T_p}$ and $\frac{V_{\alpha p}}{V_A}$ becomes more apparent as $\beta_{p\parallel}$ increases. The observations made by Helios at larger distances from the Sun differ from those made by PSP. In Figures 3(f) and (j), $\frac{T_\alpha}{T_p}$ is not high at $V_{\alpha p}>0.5V_A$. Additionally, $\frac{T_\alpha}{T_p}$ exhibits a minimum value when $V_{\alpha p}\sim 0$ and reaches a maximum when $V_{\alpha p}\sim 0.3$–$0.5V_A$ for $R<0.5$ au (Figure 3(f)). Nevertheless, $\frac{T_\alpha}{T_p}$ is high when $V_{\alpha p}<0.5V_A$ for $R>0.5$ au, and there is no temperature ratio dip observed when $V_{\alpha p}\sim 0$ (Figure 3(j)). The observations from Helios at $R>0.5$ au are consistent with the measurements by Wind at 1 au (J. C. Kasper et al. 2013).

Figure 3(a) shows that $V_{\alpha p}$ measured by PSP is more concentrated in the range of $[-0.5, 0]V_A$ when $\beta_{p\parallel}$ is low (e.g., $\beta_{p\parallel}\sim 0.1$). With an increase in $\beta_{p\parallel}$ from less than 0.1 to greater than 1.0, the range of $V_{\alpha p}$ also increases to $[-1, 1]V_A$ or beyond. We observe that $T_{\alpha\parallel}$ is generally higher than $T_{\alpha\perp}$ in regions with low $\beta_{p\parallel}$ and high $\frac{V_{\alpha p}}{V_A}$ (Figure 3, third column). Figure 3(c) indicates that $T_{\alpha\perp}$ is generally greater than $T_{\alpha\parallel}$ at high $\beta_{p\parallel}$, which is consistent with the result shown in Figure 2(g) for $R>0.25$ au. The fourth column of Figure 3 shows that $T_{p\perp}$ is significantly greater than $T_{p\parallel}$ at high $\frac{V_{\alpha p}}{V_A}$. When $\beta_{p\parallel}$ is relatively low, $\frac{T_{p\perp}}{T_{p\parallel}}>1$ appears on average at relatively low $\frac{V_{\alpha p}}{V_A}$. PSP, Helios, and Wind have all observed these characteristics of proton temperature anisotropy with respect to $\beta_{p\parallel}$ and $\frac{V_{\alpha p}}{V_A}$. Furthermore, Helios data indicate a higher $\frac{T_{p\perp}}{T_{p\parallel}}$ than that observed in PSP data, which should be because the Helios proton temperature anisotropy data only consider the core distribution without taking the beam into account (D. Stansby et al. 2019).

Figure 4 shows the distribution of $\frac{V_{\alpha p}}{V_A}$ and $\frac{T_\alpha}{T_p}$ observed by PSP and Helios at different distances from the Sun. PSP's results near the Sun indicate a positive correlation between $\frac{T_\alpha}{T_p}$ and $\left|\frac{V_{\alpha p}}{V_A}\right|$. In particular, $\frac{T_\alpha}{T_p}$ reaches a minimum value when $\frac{V_{\alpha p}}{V_A}\sim 0$ and increases with $\left|\frac{V_{\alpha p}}{V_A}\right|$ (Figure 4(a)). In contrast, the Helios results beyond 0.29 au reveal a negative correlation between $\frac{T_\alpha}{T_p}$ and $\left|\frac{V_{\alpha p}}{V_A}\right|$ (Figures 4(b) and (c)). Therefore, the correlation between $\frac{T_\alpha}{T_p}$ and $\left|\frac{V_{\alpha p}}{V_A}\right|$ varies considerably with the radial distance, transitioning from a positive correlation within the effective measurement distance range of PSP to a negative correlation within the effective measurement distance range of Helios. Within a certain range of $\left|\frac{V_{\alpha p}}{V_A}\right|$, we perform a linear fit between $\left|\frac{V_{\alpha p}}{V_A}\right|$ and $\frac{T_\alpha}{T_p}$ and obtain the following three results:

$$\frac{T_\alpha}{T_p}=4.2+4.3\left|\frac{V_{\alpha p}}{V_A}\right|,\ \text{(PSP)}, \tag{12}$$

$$\frac{T_\alpha}{T_p}=8.6-4.9\left|\frac{V_{\alpha p}}{V_A}\right|,\ \text{(Helios}<0.5\ \text{au)}, \tag{13}$$

$$\frac{T_\alpha}{T_p}=9.8-5.6\left|\frac{V_{\alpha p}}{V_A}\right|,\ \text{(Helios}>0.5\ \text{au)}. \tag{14}$$

We believe that this negative correlation detected by Helios is caused by an instability that limits the solar wind drift speed (see the black dashed curves in Figures 4(b) and (c) and discussion in Section 4.1). In Section 3.3, we show that this limitation occurs mainly in fast wind. In contrast, PSP does not observe the negative correlation between $\left|\frac{V_{\alpha p}}{V_A}\right|$ and $\frac{T_\alpha}{T_p}$ because PSP detects mainly slow wind.

In Figures 4(d)–(f), we illustrate the distribution of the Coulomb collision number N_C in the two-dimensional parameter space of $\frac{V_{\alpha p}}{V_A}$ and $\frac{T_\alpha}{T_p}$. A clear negative correlation of $\frac{T_\alpha}{T_p}$ with N_C can be seen in both PSP and Helios data, and a negative correlation of $\frac{V_{\alpha p}}{V_A}$ with N_C can also be seen in the Helios data. The data from Helios can be divided into two parts based on the value of N_C. In the high N_C solar wind, $\frac{V_{\alpha p}}{V_A}$ and $\frac{T_\alpha}{T_p}$ have on average small values. In contrast, the low N_C solar wind has on average relatively large $\frac{V_{\alpha p}}{V_A}$ or $\frac{T_\alpha}{T_p}$, which are anticorrelated with each other. However, for the data obtained from PSP, even if N_C is large, $\frac{V_{\alpha p}}{V_A}$ and $\frac{T_\alpha}{T_p}$ can be large. Compared to the Helios spacecraft, which operates at a larger heliocentric distance, PSP observes a higher N_C, which might result from the fact that PSP

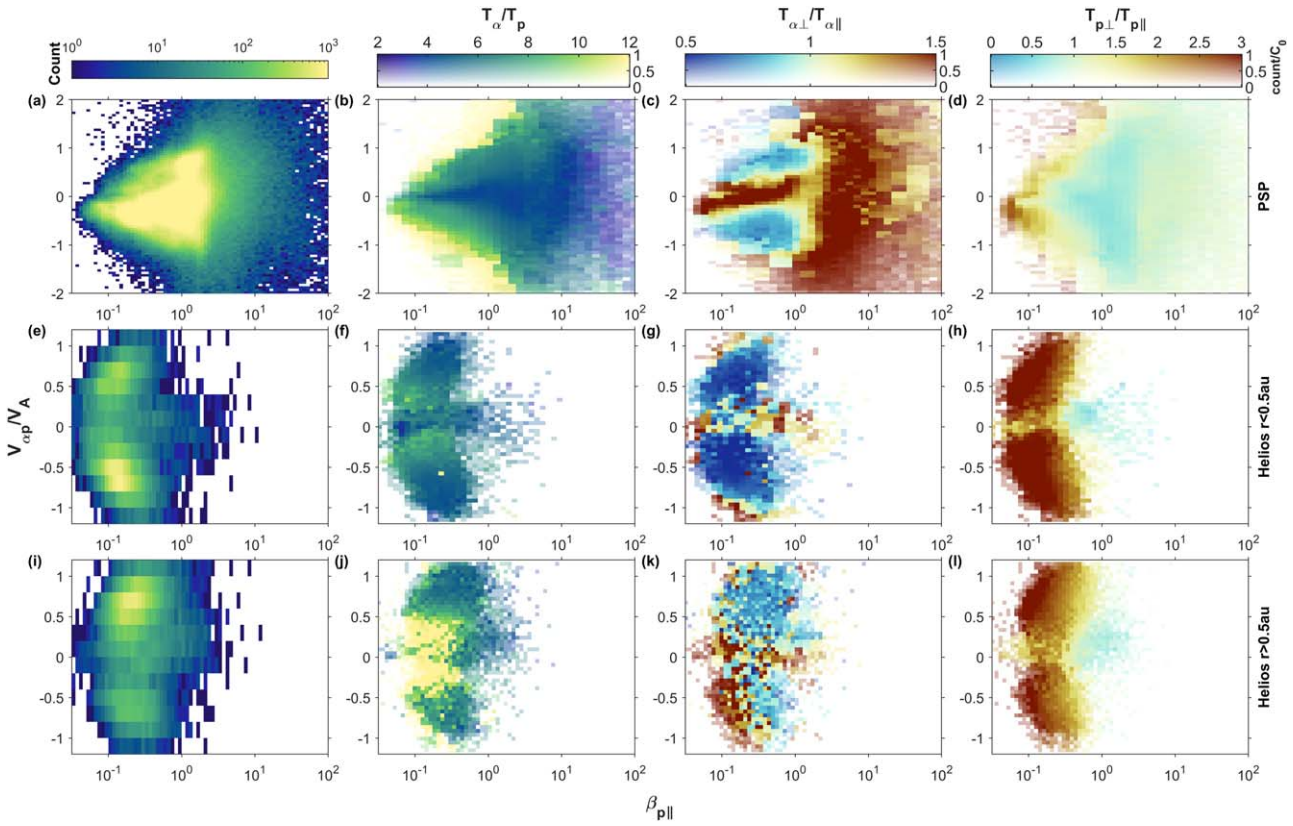

Figure 3. Distribution of data in ($\beta_{p\parallel}$, $V_{\alpha p}$) space. The three rows represent the results from PSP, Helios within 0.5 au, and Helios beyond 0.5 au, respectively. From left to right, the four columns represent the number of counts in each bin, the bin-averaged temperature ratio, the bin-averaged α-particle temperature anisotropy, and the bin-averaged proton temperature anisotropy. For the last three columns, the color saturation represents the ratio of the count number to a threshold count number (C_0), with $C_0 = 100$ for PSP data and $C_0 = 10$ for Helios data.

mostly observes slow solar wind streams at higher densities. This is discussed in Sections 3.3 and 4.1.

3.3. Differential Distributions of Drift Speed and Temperature Ratio in Fast and Slow Solar Wind

In Section 3.2, we observe a difference in the distributions of $\frac{V_{\alpha p}}{V_A}$ and $\frac{T_\alpha}{T_p}$ as detected by PSP and Helios. In particular, the two are positively correlated in the PSP data, while they exhibit a negative correlation in the Helios data. To further analyze the reason for this difference, we show the $V_{\rm pr}$ profiles detected by PSP and Helios in Figure 5 and denote the Coulomb collision number $N_{\rm C}$ by color. As we can see, PSP mainly detects slow wind ($V_{\rm pr} < 500\,{\rm km\,s^{-1}}$), while Helios mainly detects fast wind ($V_{\rm pr} > 500\,{\rm km\,s^{-1}}$). Therefore, even though PSP is closer to the Sun than Helios, the slow wind it detects still undergoes more Coulomb collisions compared to the farther fast wind detected by Helios.

Figures 6(a) and (b) show the distribution of $\frac{V_{\alpha p}}{V_A}$ and $\frac{T_\alpha}{T_p}$ for different $V_{\rm pr}$. For the PSP data, which is mostly recorded during intervals of slow wind, we find a positive correlation between $\frac{V_{\alpha p}}{V_A}$ and $\frac{T_\alpha}{T_p}$. Similarly, in the slow wind ($V_{\rm pr} < 500\,{\rm km\,s^{-1}}$) part of the Helios data, we find the same positive correlation as in the PSP data. However, in the fast wind ($V_{\rm pr} > 500\,{\rm km\,s^{-1}}$) part of the Helios data, we find an anticorrelation between $\frac{V_{\alpha p}}{V_A}$ and $\frac{T_\alpha}{T_p}$.

In Figures 6(c) and (d), we show that the distribution of Helios fast wind data in $\frac{V_{\alpha p}}{V_A}$–$\frac{T_\alpha}{T_p}$ space fits well with the predicted instability threshold curves. As the PSP data are mostly slow wind, the drift speed does not reach the instability threshold. Combining Figures 4(e) and (f) and 6(d), for the Helios data, the distribution in $\frac{V_{\alpha p}}{V_A}$–$\frac{T_\alpha}{T_p}$ space is well separated by $N_{\rm C}$ into two parts: the fast wind has a lower number of collisions, and $\frac{V_{\alpha p}}{V_A}$ and $\frac{T_\alpha}{T_p}$ are larger, forming a "butterfly" distribution. The slow wind has a higher number of collisions and lower $\frac{V_{\alpha p}}{V_A}$ and $\frac{T_\alpha}{T_p}$. However, for the data obtained from PSP, even if $N_{\rm C}$ is large, the drift speed and temperature ratio can be large.

Figures 6(e) and (f) show the nonthermal properties in the solar wind with respect to the dimensionless magnetic field perturbation $\frac{\delta B}{B_0}$. In the Helios data, $\frac{V_{\alpha p}}{V_A}$ and $\frac{T_\alpha}{T_p}$ are positively correlated with $\frac{\delta B}{B_0}$. In addition, in the PSP data, there is a clear positive correlation between $\frac{V_{\alpha p}}{V_A}$ and $\frac{\delta B}{B_0}$, but the relationship between $\frac{T_\alpha}{T_p}$ and $\frac{\delta B}{B_0}$ is not obvious. This indicates that the magnetic field perturbation strength is also a parameter that affects the drift speed and temperature ratio.

Figure 7 shows the difference in temperature anisotropy in fast and slow wind. In the fast solar wind measured by PSP, α-particles exhibit a higher perpendicular temperature compared to their parallel temperature (Figure 7(a)). In contrast, in the slow solar wind with a higher $N_{\rm C}$, α-particles have a higher perpendicular temperature, while in the slow solar wind with a lower $N_{\rm C}$, the parallel temperature is greater than the perpendicular temperature (Figure 7(a)). Helios measurements in fast wind show that α-particles have a higher parallel temperature than

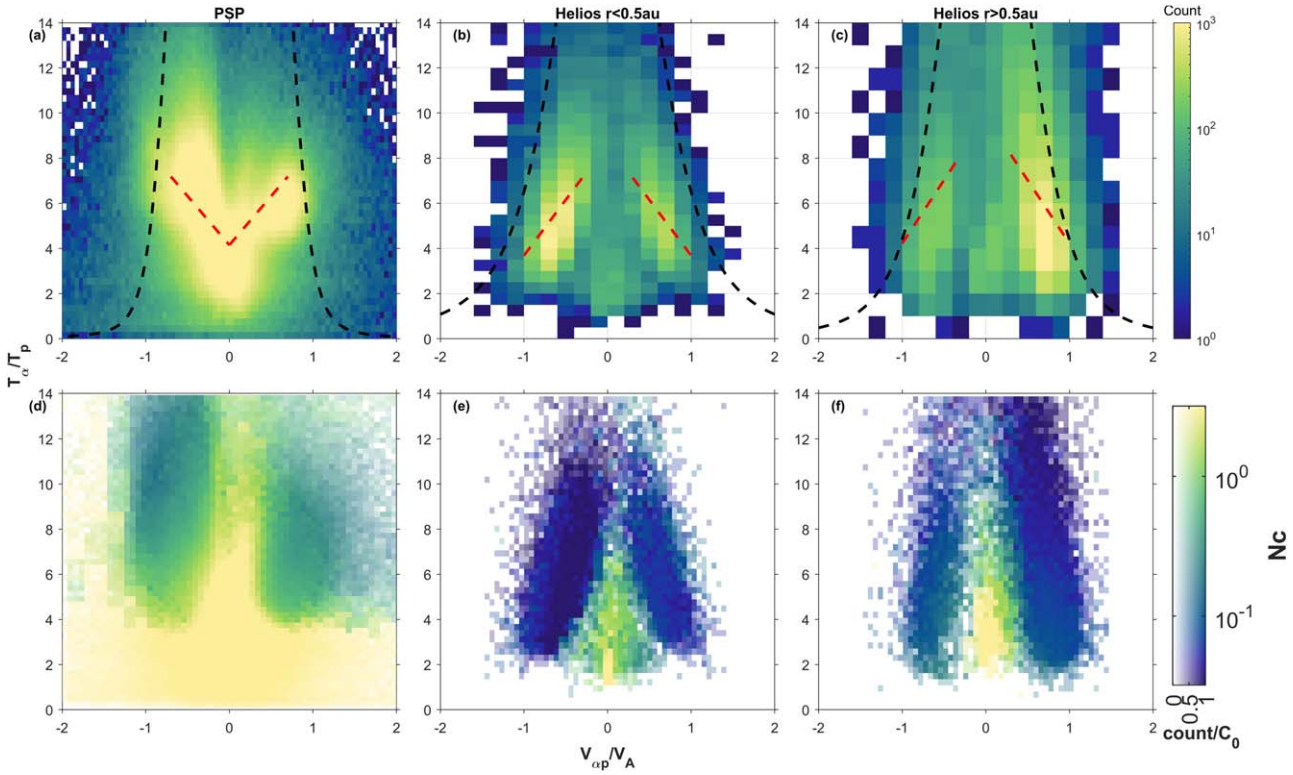

Figure 4. Distribution in the two-dimensional parameter space of $\frac{V_{\alpha p}}{V_A}$ and $\frac{T_\alpha}{T_p}$ as observed by PSP and Helios at different heliocentric distances. The color in the first row indicates the number of counts in each bin, while the color in the second row indicates the logarithm of the Coulomb collision number N_C, and the color saturation indicates the ratio of the count number to a threshold count number (C_0), with $C_0 = 100$ for PSP data and $C_0 = 10$ for Helios data. The three columns from left to right correspond to the results of PSP, Helios within 0.5 au, and Helios beyond 0.5 au. The red dotted lines in (a)–(c) represent the linear fit results for $\frac{T_\alpha}{T_p}$ and $\left|\frac{V_{\alpha p}}{V_A}\right|$, this fit is performed within the range of $\left|\frac{V_{\alpha p}}{V_A}\right|$ marked by the red dashed line. The black dashed curves in (a), (b), and (c) represent isocontours of constant maximum growth of the FM/W instability in terms of the drift speed, which are plotted based on Equation (29) with the parameters $\beta_{p\parallel}$ and $\frac{T_{\alpha\perp}}{T_{\alpha\parallel}}$ being adopted in line with the average PSP/Helios observations in each bin, and we set $\frac{n_\alpha}{n_p}$ to 0.05.

perpendicular temperature. In the slow, collision-rich solar wind, the perpendicular temperature of α-particles is higher (Figure 7(b)). According to Figures 7(c) and (d), the anisotropy characteristics of the proton temperature measured by the PSP and Helios spacecraft are quite similar: in the slow, collision-rich solar wind, the parallel temperature of protons is higher, and the opposite is true for the fast, collision-poor solar wind. In the slow, collision-rich solar wind, the higher perpendicular temperature of α-particles may be attributed to preferential heating of α-particles through wave–particle interactions. In the fast streams detected by Helios, the higher parallel temperature of α-particles and the higher perpendicular temperature of protons are qualitatively consistent with the simulation results of S. P. Gary et al. (2003) and can be explained by the presence of instabilities excited by large drift velocities in fast streams that stimulate wave fluctuations. Additionally, the higher parallel temperature of α-particles in high-speed streams can also be explained by the parallel heating mechanisms mentioned in Section 3.1, such as the forward cascade and dissipation of decaying kinetic Alfvénic turbulence.

In Helios observations, the opposite behavior of proton thermal anisotropy and α-particle thermal anisotropy differs from the findings of the Wind spacecraft, which show a positive correlation between the temperature anisotropy of protons and α-particles (B. A. Maruca et al. 2012). This discrepancy may be due to the fact that the Wind data analysis does not distinguish between the core and beam of protons, whereas the Helios data consider only the temperature of the proton core.

3.4. Zones of Preferential Heating and Acceleration for Heavy Ions

J. C. Kasper et al. (2017) suggest that the outer boundary of the solar wind's preferential heating zone may lie between $20R_{\rm Sun}$(0.09 au) and 40 $R_{\rm Sun}$(0.19 au) and may be crossed by PSP. In this section, we discuss methods for identifying the boundaries of the zones of preferential heating and acceleration and use the data from PSP to do so.

3.4.1. Zone of Heavy Ion Preferential Heating

We consider the effects of expansion, heating, and collisions on the temperature for ion species s ($s = \alpha, p$) and express the steady-state internal energy equation similar to J. C. Kasper et al. (2017),

$$\frac{dT_s}{dr} = (\gamma - 1)\left[\frac{T_s}{n_s}\frac{dn_s}{dr} + \frac{Q_s}{n_s k_{\rm B} u}\right] - \sum_{s'}\frac{\nu_{ss'}}{u}(T_s - T_{s'}), \quad (15)$$

where Q_s is the heat input of the ion species s per unit volume and per unit time, $\nu_{ss'}$ is the Coulomb collision frequency between species s and s', and u is the solar wind bulk speed. The adiabatic index γ is assumed to be $\frac{5}{3}$.

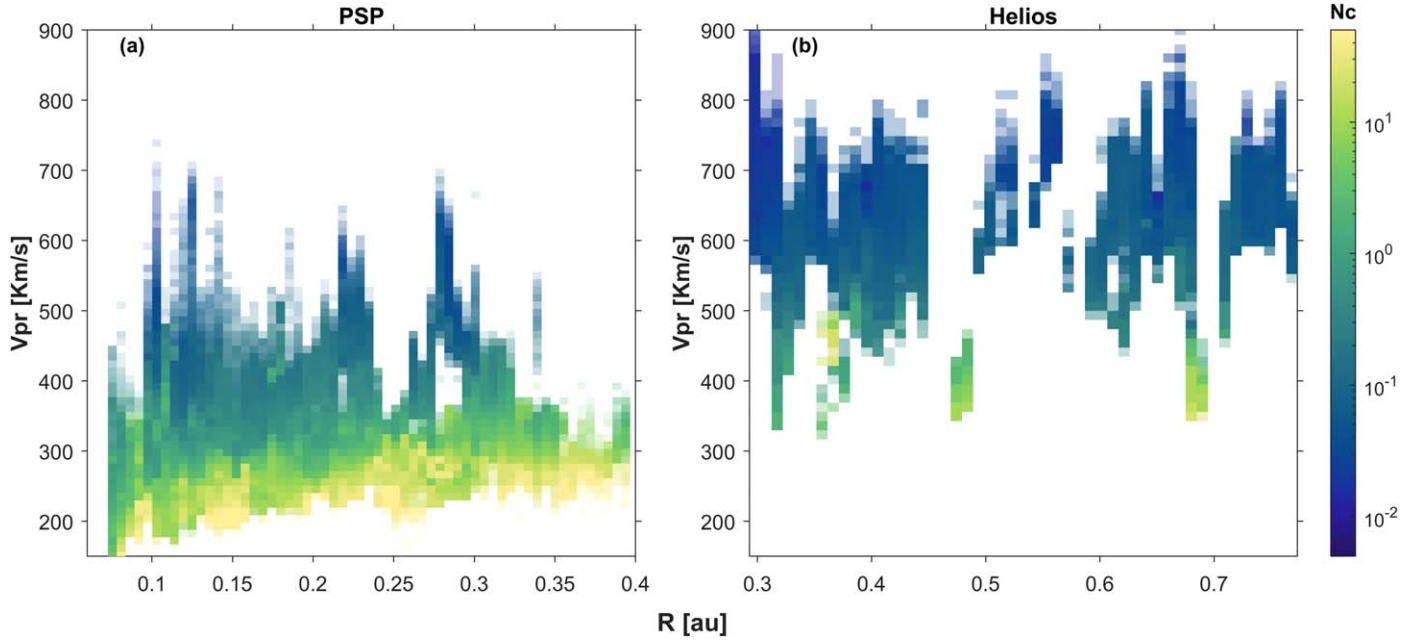

Figure 5. Radial evolution of Coulomb collision number N_C and proton radial velocity V_{pr}. Data from PSP and Helios both indicate that as V_{pr} increases, N_C decreases. Most of the V_{pr} detected by PSP is less than 500 km s^{-1}, while Helios detects a majority of wind streams with speeds greater than 500 km s^{-1}.

The equation for the radial evolution of the temperature ratio $\epsilon = \frac{T_\alpha}{T_p}$ can be written as

$$\begin{aligned}\frac{d\epsilon}{dr} &= \frac{1}{T_p}\frac{dT_\alpha}{dr} - \frac{T_\alpha}{T_p^2}\frac{dT_p}{dr} \\ &= \frac{\gamma-1}{T_p}\left[\frac{T_\alpha}{n_\alpha}\frac{dn_\alpha}{dr} - \frac{T_\alpha}{n_p}\frac{dn_p}{dr} + \frac{Q_\alpha}{n_\alpha k_B u} - \frac{T_\alpha}{T_p}\frac{Q_p}{n_p k_B u}\right] \\ &\quad - \frac{T_\alpha - T_p}{T_p}\left[\frac{\nu_{\alpha p}}{u} + \frac{\nu_{p\alpha}}{u}\frac{T_\alpha}{T_p}\right].\end{aligned} \tag{16}$$

We assume that the number density of ion species s decreases radially with a power law,

$$n_s(r) = n_{0s}\left(\frac{R_0}{r}\right)^{\xi_s}, \tag{17}$$

where n_{0s} are the number density for ion species s at a reference position R_0. According to Equations (1) and (2), the power indexes for α-particles and protons are set to $\xi_\alpha = 3.2$ and $\xi_p = 2.68$. Then, the evolution of the temperature ratio in Equation (16) has three contributions: expansion term, heating term, and collision term:

$$\begin{aligned}\frac{d\epsilon}{dr} &= (\gamma-1)(\xi_p - \xi_\alpha)\frac{\epsilon}{r} + \frac{\gamma-1}{T_p k_B u}\left[\frac{Q_\alpha}{n_\alpha} - \epsilon\frac{Q_p}{n_p}\right] \\ &\quad - \frac{\nu_{\alpha p}}{u}(\epsilon-1)(1+\epsilon F),\end{aligned} \tag{18}$$

where

$$\frac{\nu_{p\alpha}}{\nu_{\alpha p}} = \frac{n_\alpha m_\alpha}{n_p m_p} \equiv F. \tag{19}$$

Here, the first term on the right-hand side (rhs) of Equation (18) represents the effect of expansion, and since $\xi_p - \xi_\alpha < 0$, this term makes $\frac{T_\alpha}{T_p}$ decrease. The second term represents heating, and the third term represents collisions. In the preferential heating zone, the heating causes an increase in $\frac{T_\alpha}{T_p}$, while expansion and collisions cause temperature equilibration. In this study, we define the criterion for preferential heating as

$$\frac{Q_\alpha}{Q_p} > \frac{n_\alpha T_\alpha}{n_p T_p}. \tag{20}$$

From Equation (18), we can infer that: (1) if the heating term is greater than the collision and expansion term, $\frac{T_\alpha}{T_p}$ increases with the radial distance; (2) if the heating term is less than the collision term and expansion term, $\frac{T_\alpha}{T_p}$ decreases with the radial distance, but $\frac{T_\alpha}{T_p}$ should decrease more slowly than predicted for collisions and expansion only; (3) if the heating term is much smaller than the collision term and expansion term, the radial evolution of $\frac{T_\alpha}{T_p}$ should be well predicted by collisional and expansion effects alone. According to Figure 8(a), the trend of $\frac{T_\alpha}{T_p}$ with the radial distance is decreasing, suggesting that the heating term is not universally stronger than the collision term and expansion term.

By only considering the evolution of $\frac{T_\alpha}{T_p}$ due to collisions and expansion, we obtain backtracking curves of $\frac{T_\alpha}{T_p}$ in a range of [0.06, 0.36] au, based on the median and quartile values of $\frac{T_\alpha}{T_p}$ observed at approximately 0.36 au by PSP. In the backtracking calculation, we assume a constant bulk speed of $u = 300$ km s^{-1}. The backtracking curves are the blue curves in Figure 8(a). The actual radial evolution of the median of $\frac{T_\alpha}{T_p}$ does not strictly follow the backtracking curve. Within 0.16 au, the median of $\frac{T_\alpha}{T_p}$ decays more slowly with distance than predicted. This shows that within 0.16 au, the preferential heating term makes a significant contribution, comparable to the expansion and collision terms. Thus, we consider 0.16 au the outer boundary of the heavy ion preferential heating zone.

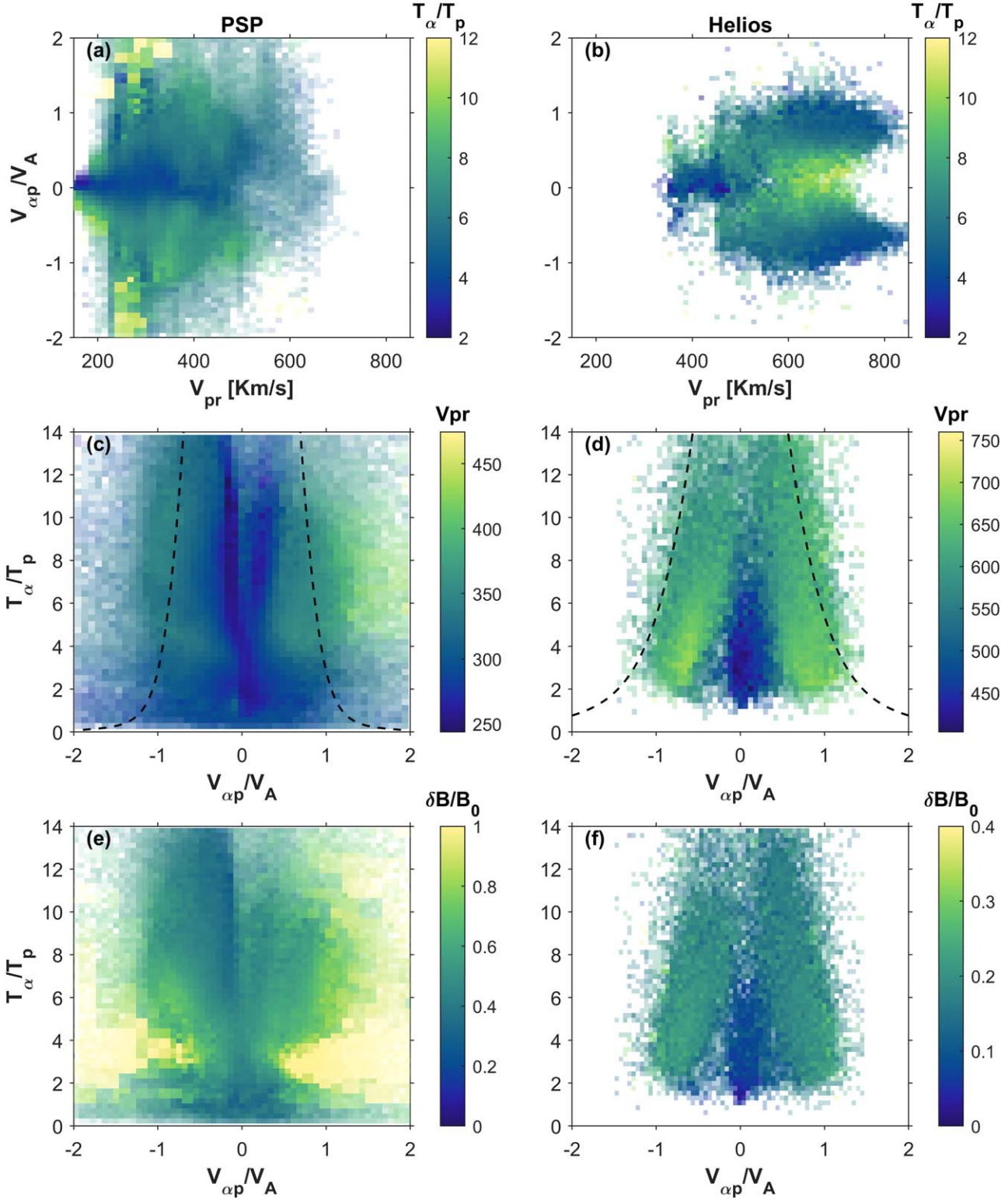

Figure 6. $\frac{T_\alpha}{T_p}$-$\frac{V_{\alpha p}}{V_A}$ distributions as a function of $V_{\rm pr}$ and $\frac{\delta B}{B_0}$. (a) and (b) the horizontal axis is the proton velocity $V_{\rm pr}$, the vertical axis is the dimensionless drift speed $\frac{V_{\alpha p}}{V_A}$, and the colors indicate $\frac{T_\alpha}{T_p}$. (c)–(f) The horizontal axis is $\frac{V_{\alpha p}}{V_A}$, and the vertical axis is $\frac{T_\alpha}{T_p}$. The colors in (c) and (d) indicate the proton velocity $V_{\rm pr}$. The black dashed curves represent isocontours of constant maximum growth of the FM/W instability in terms of $\frac{V_{\alpha p}}{V_A}$, the same as Figure 4. The colors in (e) and (f) indicate the ratio of the magnetic field perturbation standard deviation to the background magnetic field, where PSP uses magnetic field data over 30 minutes to calculate the magnetic field perturbation standard deviation, and Helios uses data over 40 s.

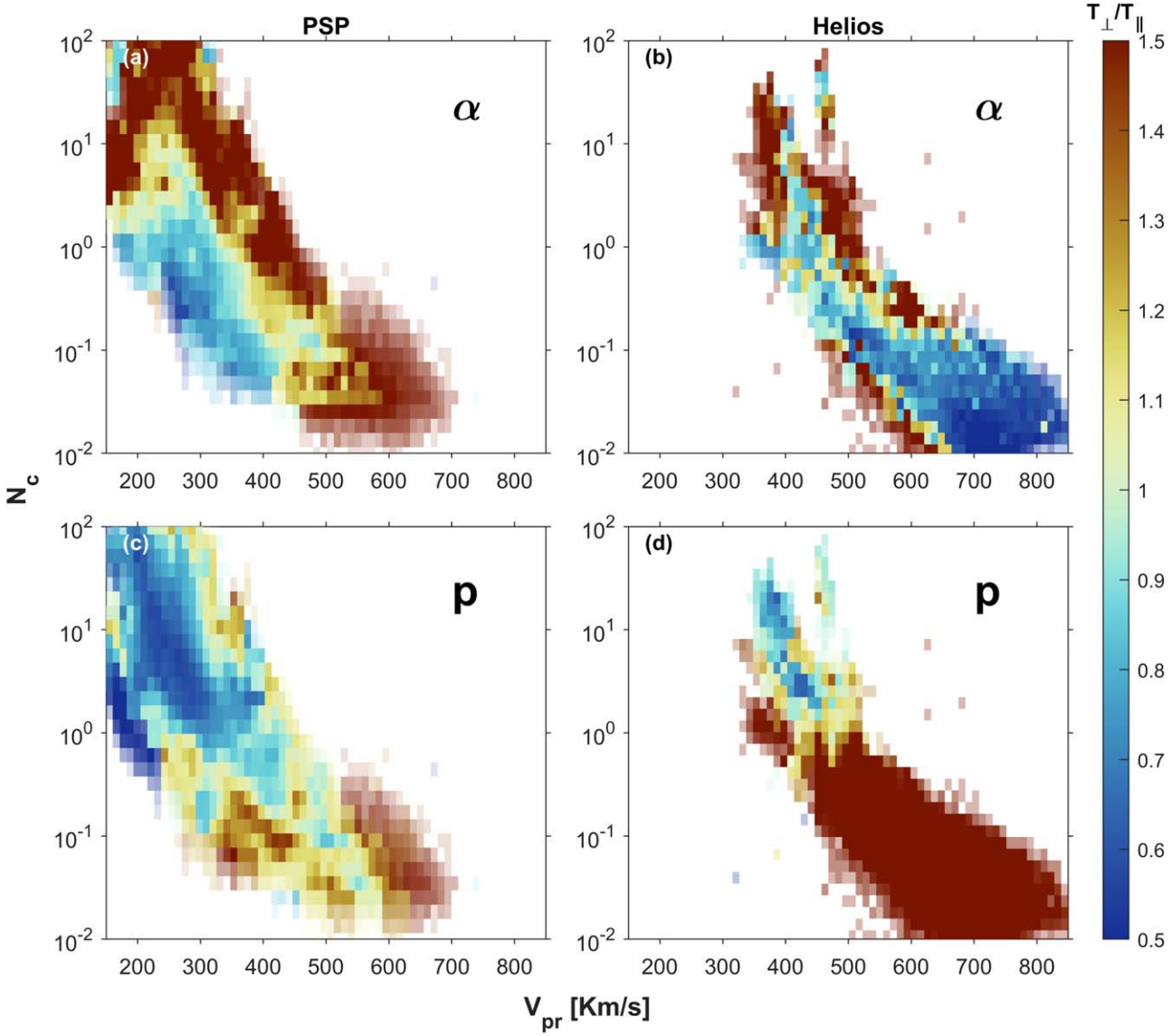

Figure 7. Temperature anisotropy of α-particles and protons in $V_{\rm pr}$–$N_{\rm C}$ space. (a) and (c) present PSP data, while (b) and (d) show Helios data. The color bar indicates the ratio of $\frac{T_\perp}{T_\parallel}$.

3.4.2. Zone of Heavy Ion Preferential Acceleration

Considering the radial momentum equation for species s ($s = \alpha$, p) in a steady wind,

$$\frac{1}{2}\frac{dv_s^2}{dr} = -\frac{1}{n_s m_s}\frac{dp_s}{dr} - \frac{Z_s}{n_e m_s}\frac{dp_e}{dr} - \frac{GM_{\rm sun}}{r^2} + a_s + \frac{d}{dr}\left[\frac{p_w}{\rho v_{\rm Ar}^2}(v_{\rm ph}^2 - v_s^2)\right] - \sum_{s'}\nu_{ss'}(v_s - v_{s'}), \tag{21}$$

where v_s, p_s, and Z_s are the radial velocity, the ion pressure, and the nuclear charge for species s, respectively. p_e is the electron pressure, p_w is the wave pressure, $M_{\rm Sun}$ is the solar mass, $v_{\rm Ar}$ is the radial Alfvén velocity, and $v_{\rm ph}$ is the Alfvén wave radial phase velocity.

The terms on the rhs of Equation (21) are the ion pressure gradient force, the electron pressure gradient, the solar gravity, the acceleration due to wave/turbulence-related field–particle interaction a_s, the wave pressure gradient force, and the effect of ion-ion collisions (Y. Q. Hu & S. R. Habbal 1999). By subtracting the momentum equation for protons from that for α-particles, we obtain the radial evolution equation for the difference in velocity squares of α-particles and protons:

$$\frac{1}{2}\frac{d}{dr}(v_\alpha^2 - v_p^2) = -\left(\frac{1}{n_\alpha m_\alpha}\frac{dp_\alpha}{dr} - \frac{1}{n_p m_p}\frac{dp_p}{dr}\right) + \frac{1}{2n_e m_p}\frac{dp_e}{dr} + (a_\alpha - a_p) - \frac{d}{dr}\left[\frac{p_w}{\rho v_{\rm Ar}^2}(v_\alpha^2 - v_p^2)\right] - \nu_{\alpha p}(1+F)v_{\alpha p}. \tag{22}$$

As per the first term on the rhs of Equation (22), if the temperature ratio between α-particles and protons exceeds their mass ratio, this term can be greater than 0, leading to a preferential acceleration of α-particles compared to protons. Regarding the third term on the rhs, since the gyroperiod and thermal gyroradius of α-particles are greater than those of protons, α-particles are more likely to interact with lower-frequency,

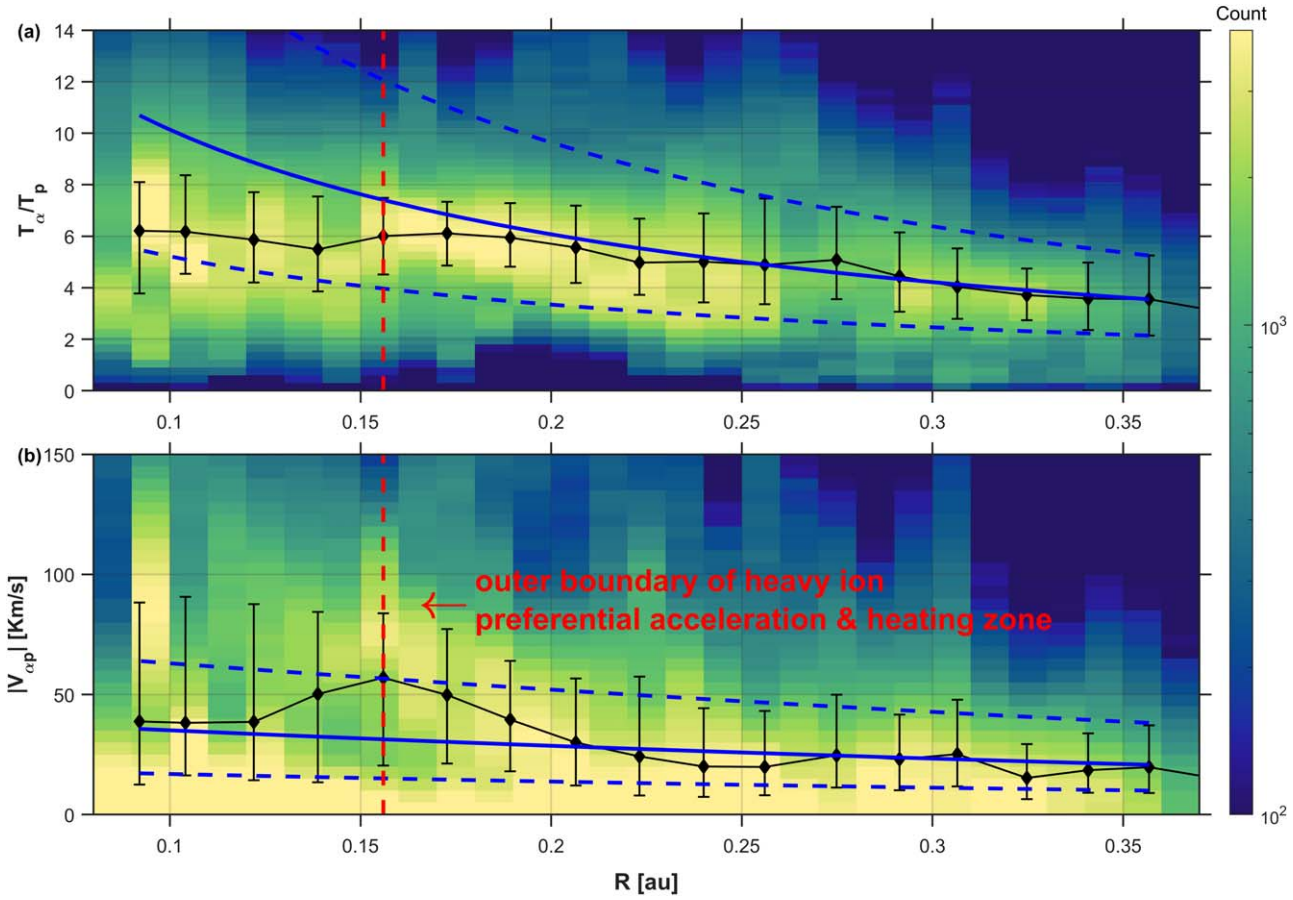

Figure 8. Radial evolution of (a) $\frac{T_\alpha}{T_p}$ and (b) $|V_{\alpha p}|$. The black solid curve represents the local median while the error bars indicate the local quartiles. The blue solid curve and blue dashed curve illustrate the results from our model given by Equations (18) and (27), which predict $\frac{T_\alpha}{T_p}$ and $V_{\alpha p}$ based on the median and quartiles of $\frac{T_\alpha}{T_p}$ and $|V_{\alpha p}|$ at 0.357 au (the rightmost error bars). (b) The red dashed line with the arrow indicates the estimated outer boundary of the preferential acceleration zone.

larger-scale fluctuations/turbulence in field–particle interactions. Regarding the fourth term on the rhs, if the bulk velocity of α-particles is greater than that of the protons, indicating an outward relative drift from the Sun, the wave pressure gradient force will decrease the drift speed. In analogy to the analysis of preferential heating for heavy ions, we reexpress the rhs of Equation (22) as a sum of two terms: the noncollisional term $A_{\alpha p}$ and a collisional term:

$$\frac{1}{2}\frac{d}{dr}(v_\alpha^2 - v_p^2) = A_{\alpha p} - \nu_{\alpha p}(1+F)v_{\alpha p}, \tag{23}$$

where

$$A_{\alpha p} = -\left(\frac{1}{n_\alpha m_\alpha}\frac{dp_\alpha}{dr} - \frac{1}{n_p m_p}\frac{dp_p}{dr}\right) + \frac{1}{2n_e m_p}\frac{dp_e}{dr} + (a_\alpha - a_p) - \frac{d}{dr}\left[\frac{p_w}{\rho v_{\rm Ar}^2}(v_\alpha^2 - v_p^2)\right]. \tag{24}$$

Notice that

$$\frac{1}{2}(v_\alpha^2 - v_p^2) = \frac{1}{2}(v_\alpha - v_p)(v_\alpha + v_p) = v_{\alpha p}(v_p + v_{\alpha p}/2) \tag{25}$$

$$\frac{1}{2}\frac{d}{dr}(v_\alpha^2 - v_p^2) = (v_{\alpha p} + v_p)\frac{dv_{\alpha p}}{dr} + v_{\alpha p}\frac{dv_p}{dr}. \tag{26}$$

As before, we assume a constant proton speed $v_p = 300\ \mathrm{km\ s^{-1}}$. Equation (23) simplifies to

$$\frac{dv_{\alpha p}}{dr} = \frac{A_{\alpha p}}{v_{\alpha p} + v_p} - \nu_{\alpha p}(1+F)\frac{v_{\alpha p}}{v_{\alpha p} + v_p}. \tag{27}$$

We define the criterion for preferential acceleration as

$$A_{\alpha p} > 0. \tag{28}$$

For the corresponding backtracking, we neglect the first term on the rhs of Equation (27), and begin the backtracking around 0.36 au (see the blue curve in Figure 8(b)). Figure 8(b) suggests that, within 0.16 au, the preferential acceleration is stronger than the collisional relaxation of the relative drift speed. However, from 0.16 to 0.25 au, $|V_{\alpha p}|$ decreases rapidly, with the declining trend exceeding the predicted trend based on collisions. This implies that other mechanisms besides collisions are likely to reduce the drift speed at these locations, such as drift instabilities (S. P. Gary et al. 2000a, 2000b, 2003; Q. Lu et al. 2006; D. Verscharen et al. 2013, 2015; X. Zhu et al. 2023). Also, the shift of the bin center to higher drift speeds in the range of [0.12, 0.2] au could be due to PSP crossing into another wind stream with different speeds (see discussion in Section 4.2). Therefore, we estimate that the outer boundary of the preferential acceleration zone is at a distance of around 0.16 au.

4. Discussion

4.1. Mechanisms That Affect the Heavy Ion–Proton Drift Speed and Temperature Ratio

Our PSP and Helios observations suggest that the distribution of the drift speed and temperature ratios varies considerably in the fast and slow wind. In the fast wind, we find a positive correlation between $\frac{V_{\alpha p}}{V_A}$ and $\frac{T_\alpha}{T_p}$, while in the slow wind, they are negatively correlated. To explain this difference, we discuss some mechanisms that can cause changes in the drift speed and temperature ratios.

Magnetic reconnection. J. F. Drake et al. (2009) simulate ion heating during the reconnection process and find that the temperature of ions rapidly increases upon crossing the boundary between the upstream plasma and the reconnection exhaust region. J. F. Drake et al. (2009) propose that the efficient energization mechanism for ions in the reconnection exhaust region (especially in areas where slow shocks do not form) is pickup energization, which involves ions entering the exhaust region and rapidly acquiring energization from the fast-convected reconnected magnetic field. Theoretical analysis suggests that the increase in internal energy of ions is given by $\frac{1}{3}m_i v_0^2$, where v_0 represents the flow speed of the proton reconnection jet flow and m_i is the mass of the ion species. Satellite observations from missions such as Wind, ACE, and Solar Orbiter indicate that the change in the ion temperature is approximately proportional to the mass of the species (J. F. Drake et al. 2009; D. Duan et al. 2023). Measurements from Wind have shown that the temperature change is proportional to the square of the outflow speed, although it is smaller than predicted by J. F. Drake et al. (2009). Studies investigate the acceleration effect of oxygen ions during magnetic reconnection in the magnetotail (Y. H. Liu et al. 2015; H. Liang et al. 2017; T. Wu 2020). Oxygen ions, having a larger gyroradius than protons at the same energy, experience more acceleration by reconnection electric fields in the diffusion region than protons.

Wave–particle interactions. Turbulent field fluctuations in the solar wind can transfer energy to particles through field–particle interactions. The uneven distribution of this energy among different species may be a mechanism inducing preferential heating and acceleration of heavy ions. Figure 6(f) shows that for Helios data, the larger $\frac{\delta B}{B_0}$, the larger are $\frac{V_{\alpha p}}{V_A}$ and $\frac{T_\alpha}{T_p}$. In addition, for the PSP data in Figure 6(e), there is a clear positive correlation between $\frac{V_{\alpha p}}{V_A}$ and $\frac{\delta B}{B_0}$. Here, we use $\frac{\delta B}{B_0}$ to indicate the strength of the wave–particle interaction (S. P. Gary et al. 2001). This observation provides evidence that wave–particle interactions preferentially heat and accelerate heavy ions. When the drift speed is less than a critical value of about $0.2V_A$, ICWs can result in field–particle interactions that preferentially heat and accelerate heavy ions (S. P. Gary et al. 2001). This mechanism accelerates α-particles to an order of V_A faster than protons and heats them to temperatures above the mass ratio, within a few solar radii from the solar surface (Y. Q. Hu & S. R. Habbal 1999). However, as the drift speed exceeds the critical value at further distances from the Sun, the influence of heavy ions on the wave dispersion relation results in the preferential heating of protons and a reduction in drift speed. The positive correlation between the drift speed and temperature ratio observed by PSP and Helios in slow wind may be a result of preferential heating and acceleration of α-particles due to field–particle interactions.

Coulomb collisions. As depicted in Figures 2(b) and (d), Coulomb collisions can effectively reduce the drift speed and temperature difference. Figure 5 shows that PSP predominantly detects slow wind, while Helios predominantly measures fast wind. Therefore, even though PSP is closer to the Sun than Helios, the slow wind it detects still undergoes more Coulomb collisions compared to the farther fast wind detected by Helios. It is reasonable to assume that an increase in the effects of collisions leads to a simultaneous reduction in $\frac{V_{\alpha p}}{V_A}$ and $\frac{T_\alpha}{T_p}$, so we believe that collisions may be one reason for the positive correlation between $\frac{V_{\alpha p}}{V_A}$ and $\frac{T_\alpha}{T_p}$ in slow wind.

Plasma instability. When the drift speed exceeds a certain threshold, wave instability can be triggered, resulting in the transfer of kinetic energy from α-particles to wave fields. D. Verscharen et al. (2015) show that the FM/W instability constraints the α-particle drift speed near the instability threshold, which is given by

$$\begin{aligned}\frac{U_{\mathrm{FM/W}}}{V_A} &= 1 - \sigma_2\left(1 - \frac{T_{\alpha\perp}}{T_{\alpha\parallel}}\right)\frac{w_{\alpha\parallel}}{V_A} + \frac{1}{4\sigma_2}\frac{V_A}{w_{\alpha\parallel}}\frac{T_{\alpha\parallel}}{T_{\alpha\perp}} \\ &= 1 - \sigma_2\left(1 - \frac{T_{\alpha\perp}}{T_{\alpha\parallel}}\right)\frac{w_{p\parallel}}{V_A}\sqrt{\frac{T_{\alpha\parallel}}{T_{p\parallel}}\frac{m_p}{m_\alpha}} \\ &\quad + \frac{1}{4\sigma_2}\frac{1}{\frac{w_{p\parallel}}{V_A}\sqrt{\frac{T_{\alpha\parallel}}{T_{p\parallel}}\frac{m_p}{m_\alpha}}}\frac{T_{\alpha\parallel}}{T_{\alpha\perp}} \\ &= 1 - \sigma_2\left(1 - \frac{T_{\alpha\perp}}{T_{\alpha\parallel}}\right)\sqrt{\beta_{p\parallel}\frac{T_{\alpha\parallel}}{T_{p\parallel}}\frac{m_p}{m_\alpha}} \\ &\quad + \frac{1}{4\sigma_2}\frac{1}{\sqrt{\beta_{p\parallel}\frac{T_{\alpha\parallel}}{T_{p\parallel}}\frac{m_p}{m_\alpha}}}\frac{T_{\alpha\parallel}}{T_{\alpha\perp}}. \end{aligned} \tag{29}$$

Here, $w_{s\parallel} = \sqrt{2k_B T_{s\parallel}/m_s}$ represents the parallel thermal velocity of species s, and $\sigma_2 = \sqrt{-\ln\frac{M_2 n_p}{n_\alpha}}$, $M_2 = 6.1 \times 10^{-4}$. We approximate $\frac{T_{\alpha\parallel}}{T_{p\parallel}}$ in Equation (29) as $\frac{T_\alpha}{T_p}$ and plot the threshold curve of drift speed in $(\frac{V_{\alpha p}}{V_A}, \frac{T_\alpha}{T_p})$ space, as the black dashed curves in Figures 4(a), (b), and (c) and Figures 6(c) and (d). The values of $\beta_{p\parallel}$ and $\frac{T_{\alpha\perp}}{T_{\alpha\parallel}}$ are taken from the median of PSP/Helios data, and $\frac{n_\alpha}{n_p} = 0.05$ is assumed. The larger the value of $\frac{T_\alpha}{T_p}$, the lower is the threshold drift speed. This relationship is consistent with the anticorrelation between $\frac{V_{\alpha p}}{V_A}$ and $\frac{T_\alpha}{T_p}$ observed in the Helios fast wind data (Figures 4(b) and (c)). However, the distribution of the PSP-detected solar wind in $(\frac{V_{\alpha p}}{V_A}, \frac{T_\alpha}{T_p})$ space does not reach the drift speed threshold curve (Figure 4(a)). We hypothesize that most of the solar wind observed by PSP is not yet limited by wave instabilities because its α-particle drift speed is still below the threshold.

4.2. Different Solar Wind Streams Observed by PSP

In Figures 1(c)–(d), a number of branches with different speeds can be recognized within 0.1 au or in the range of

[0.2, 0.3] au. For example, considering the range of [0.2, 0.3] au, in Figure 1(c), there are three branches with $V_{\alpha r}$ of about 700 km s^{-1}, 500 km s^{-1}, and 300 km s^{-1}, respectively, and in Figure 1(d), there are three branches with $V_{\rm pr}$ of about 500 km s^{-1}, 400 km s^{-1}, and 300 km s^{-1}. Similar branches with different $T_{\alpha\perp}$ can be discerned in Figure 1(e). In Figure 8(b), within 0.2 au, two branches with high and low drift speeds appear. At 0.15 au, the branches with high and low drift speeds have drift speeds of about 100 km s^{-1} and 10 km s^{-1}, respectively. Within the heavy ion preferential acceleration zone (within 0.16 au), the branch with low drift speeds still dominates.

We suggest that the different branches may be due to PSP entering streams with different properties. In different encounters, PSP detects different solar wind streams, and in the same encounter, PSP may cross into another wind stream with different speeds and temperatures.

5. Conclusions

We analyze the distributions of the α-particle drift speed $V_{\alpha p}$ and α-to-proton temperature ratio $\frac{T_\alpha}{T_p}$, using PSP data at distances of 0.06–0.4 au and Helios data at distances of 0.29–0.78 au from the Sun. Our analysis suggests that preferential heating and acceleration of heavy ions coexist in slow wind, whereas in fast wind away from the Sun, the coexistence is absent. We deduce that the negative correlation between $\frac{V_{\alpha p}}{V_{\rm A}}$ and $\frac{T_\alpha}{T_p}$ in fast wind is attributed to a wave instability limiting the drift speed to a threshold value. The average drift speed and temperature ratios are larger in fast wind, where the drift speed is more likely to reach an instability threshold. In slow wind, the drift speed is usually below the threshold, so instability has no effect on the distributions of $\frac{V_{\alpha p}}{V_{\rm A}}$ and $\frac{T_\alpha}{T_p}$. Coulomb collisions contribute more significantly in slow wind, where they effectively reduce both drift the speed and the temperature ratio. Thus, one possible explanation for the positive correlation between $\frac{V_{\alpha p}}{V_{\rm A}}$ and $\frac{T_\alpha}{T_p}$ in slow wind is Coulomb collisions. Another possible reason is that preferential wave–particle heating and acceleration coexist in slow wind, which is consistent with the idea that the mechanism of heavy ion preferential heating and acceleration is active in both fast and slow wind (J. C. Kasper et al. 2017).

Our analysis shows that $\frac{T_\alpha}{T_p}$ detected by PSP generally decreases with the radial distance. However, heavy ion preferential heating mechanisms can be comparable to collisions and expansion inside 0.16 au, and we identify the outer boundary of the preferential heating zone at approximately 0.16 au, within which $\frac{T_\alpha}{T_p}$ decreases more slowly than predicted for collisions and expansion along. Also, we find that $\frac{V_{\alpha p}}{V_{\rm A}}$ increases with the radial distance inside 0.16 au. Beyond 0.16 au, $\frac{V_{\alpha p}}{V_{\rm A}}$ decays with the radial distance. Thus, we also identify the outer boundary of the preferential acceleration zone at approximately 0.16 au. We note a faster decay of $\frac{V_{\alpha p}}{V_{\rm A}}$ than predicted by Coulomb collisions alone between 0.16 and 0.25 au, suggesting the presence of other mechanisms that reduce $\frac{V_{\alpha p}}{V_{\rm A}}$ in this range.

In the inner heliosphere, there are various large-scale structures in the solar wind, such as the heliospheric plasma sheet and heliospheric current sheet. The differences in the heating and acceleration characteristics of heavy ions inside and outside these structures are worth further investigation. J. Huang et al. (2023) explore the distinctions between the plasma sheet and the current sheet in the inner heliosphere. They find that the plasma sheet exhibits a thermal equilibrium state, with a relatively low differential flow of α-particles ($\frac{V_{\alpha p}}{V_{\rm A}}$). However, the relative abundance of α-particles shows a wide range of values. They further observe two states in the current sheet: one with proton thermal isotropy and the other with proton thermal anisotropy, possibly accompanied by mirror mode instability. Correspondingly, the differential flow and relative abundance of α-particles in these two states vary: low abundance and low differential flow correspond to proton thermal anisotropy, while low abundance and high differential flow correspond to proton thermal isotropy. The heating and acceleration characteristics of heavy ions in these structures and their radial distance variations are promising avenues for future exploration.

Acknowledgments

The work at Peking University is supported by the National Key R&D Program of China (2022YFF0503800 and 2021YFA0718600), by NSFC (42241118, 42174194, 42150105, and 42204166), and by CNSA (D050106). D.V. from UCL is supported by the STFC Consolidated Grant ST/W001004/1. The authors acknowledge the contributions of the Parker Solar Probe mission operations and spacecraft engineering teams at the Johns Hopkins University Applied Physics Laboratory as well as the FIELDS and SWEAP teams for the use of the data. PSP data are available on SPDF (https://cdaweb.gsfc.nasa.gov/index.html/).

Appendix
Estimation of Coulomb Collision Number $N_{\rm C}$

The Coulomb collision number $N_{\rm C}$ is defined as (R. Chhiber et al. 2016)

$$N_C = \int_{r_0}^{r} \nu_{\alpha p}(s)\frac{ds}{u(s)}.$$

In this expression, $\nu_{\alpha p}(r)$ is the Coulomb collision frequency between α-particles and protons,

$$\nu_{\alpha p}(r) = \frac{32\sqrt{\pi}}{3}\ln\Lambda\frac{e_\alpha^2 e_p^2}{m_\alpha m_p}\frac{n_p(r)}{w_{\alpha p}^3(r)}.$$

Here, e_α, e_p, m_α, and m_p are the charges and masses of α-particles and protons, respectively, $\ln\Lambda$ is the Coulomb logarithm, which we set to a constant value of 21.

The effective thermal speed $w_{\alpha p}(r)$ is defined as:

$$w_{\alpha p}(r) = \left(\frac{2k_B T_\alpha(r)}{m_\alpha} + \frac{2k_B T_p(r)}{m_p}\right)^{1/2}.$$

We model the bulk speed u based on the Parker model (E. N. Parker 1958):

$$\tilde{u}^2 - \ln(\tilde{u}^2) = 4\ln(\tilde{r}) + 4\tilde{r} - 3,$$

where $\tilde{r} = r/r_c$, $\tilde{u} = u/u_c$, $r_c = \frac{GM_\odot m_p}{4k_{\rm B}T_c}$, and $u_c = \sqrt{2k_{\rm B}T_c/m_p}$. Here, T_c is a parameter that is calculated from the observed data.

We use power laws for the radial evolution of the density $n_p(r)$ and the thermal speed $w_{\alpha p}(r)$, which are expressed as

$$n_p(r) = n_0\left(\frac{R_0}{r}\right)^p = C_1 r^{-p},$$
$$w_{\alpha p}(r) = w_0\left(\frac{R_0}{r}\right)^m = C_2 r^{-m},$$

where n_0 and w_0 are the proton number density and effective thermal speed at a reference position R_0, respectively. Substituting these equations, we obtain a simplified expression for N_C given by

$$N_C = C \times \int_{\tilde{r}_0}^{\tilde{r}} \tilde{s}^{-\alpha}\frac{d\tilde{s}}{\tilde{u}(\tilde{s})},$$

where

$$C = \frac{32\sqrt{\pi}}{3}\ln\Lambda\frac{e_\alpha^2 e_p^2}{m_\alpha m_p}\frac{n_0}{w_0^3 u_c}R_0^\alpha r_c^{1-\alpha}$$
$$= \frac{32\sqrt{\pi}}{3}\ln\Lambda\frac{e_\alpha^2 e_p^2}{m_\alpha m_p}\frac{C_1 r_c^{1-\alpha}}{C_2^3 u_c},$$

$\tilde{r}_0 = r_0/r_c$, $\alpha = p - 3m$.

In our adopted model, we assume that C_1, C_2, r_c, u_c, and C remain constant and can be derived from spacecraft data. We choose $p = 2$ and $m = 0.3$ in this study. The selection of m is based on a combination of observations by PSP (see Equations (3–8)) and Helios (P. Hellinger et al. 2011).

ORCID iDs

Jingyu Peng https://orcid.org/0000-0001-7537-5999
Jiansen He https://orcid.org/0000-0001-8179-417X
Die Duan https://orcid.org/0000-0002-6300-6800
Daniel Verscharen https://orcid.org/0000-0002-0497-1096

References

Bale, S. D., Goetz, K., Harvey, P. R., et al. 2016, SSRv, 204, 49
Berger, L., Wimmer-Schweingruber, R. F., & Gloeckler, G. 2011, PhRvL, 106, 151103
Bowen, T. A., Bale, S. D., Bonnell, J. W., et al. 2020, JGRA, 125, e27813
Cargill, P. J., & Klimchuk, J. A. 2004, ApJ, 605, 911
Chandran, B. D. G., Li, B., Rogers, B. N., Quataert, E., & Germaschewski, K. 2010, ApJ, 720, 503
Chandran, B. D. G., Verscharen, D., Quataert, E., et al. 2013, ApJ, 776, 45
Chew, G. F., Goldberger, M. L., & Low, F. E. 1956, RSPSA, 236, 112
Chhiber, R., Usmanov, A. V., Matthaeus, W. H., & Goldstein, M. L. 2016, ApJ, 821, 34
Cranmer, S. R. 2000, ApJ, 532, 1197
Cranmer, S. R. 2009, LRSP, 6, 3
Drake, J. F., Swisdak, M., Phan, T. D., et al. 2009, JGRA, 114, A05111
Duan, D., He, J., Zhu, X., et al. 2023, ApJL, 952, L11
Ďurovcová, T., Šafránková, J., Němeček, Z., & Richardson, J. D. 2017, ApJ, 850, 164
Gary, S. P., Goldstein, B. E., & Steinberg, J. T. 2001, JGR, 106, 24955
Gary, S. P., Smith, C. W., & Skoug, R. M. 2005, JGRA, 110, A07108
Gary, S. P., Yin, L., Winske, D., & Reisenfeld, D. B. 2000a, JGR, 105, 989
Gary, S. P., Yin, L., Winske, D., & Reisenfeld, D. B. 2000b, GeoRL, 27, 1355
Gary, S. P., Yin, L., Winske, D., et al. 2003, JGRA, 108, 1068
Hellinger, P., Matteini, L., Stverak, S., Travnicek, P. M., & Marsch, E. 2011, JGRA, 116, A09105
Hoeksema, J. T., Wilcox, J. M., & Scherrer, P. H. 1983, JGR, 88, 9910
Hollweg, J. V., & Isenberg, P. A. 2002, JGRA, 107, 1147
Hu, Y. Q., & Habbal, S. R. 1999, JGR, 104, 17045
Huang, J., Kasper, J. C., Larson, D. E., et al. 2023, ApJS, 265, 47
Johnson, E., Maruca, B. A., McManus, M., et al. 2023, ApJ, 950, 51
Kasper, J. C., Klein, K. G., Weber, T., et al. 2017, ApJ, 849, 126
Kasper, J. C., Lazarus, A. J., & Gary, S. P. 2008, PhRvL, 101, 261103
Kasper, J. C., Maruca, B. A., Stevens, M. L., & Zaslavsky, A. 2013, PhRvL, 110, 091102
Kasper, J. C., Stevens, M. L., Lazarus, A. J., Steinberg, J. T., & Ogilvie, K. W. 2007, ApJ, 660, 901
Liang, H., Lapenta, G., Walker, R. J., et al. 2017, JGRA, 122, 618
Liu, Y. H., Mouikis, C. G., Kistler, L. M., et al. 2015, JGRA, 120, 3535
Livi, R., Larson, D. E., Kasper, J. C., et al. 2022, ApJ, 938, 138
Lu, Q., Xia, L., & Wang, S. 2006, JGRA, 111, A09101
Marsch, E., Rosenbauer, H., Schwenn, R., Muehlhaeuser, K. H., & Neubauer, F. M. 1982, JGR, 87, 35
Maruca, B. A., Kasper, J. C., & Gary, S. P. 2012, ApJ, 748, 137
Matteini, L., Hellinger, P., Landi, S., Trávníček, P. M., & Velli, M. 2012, SSRv, 172, 373
Matthaeus, W. H., Zank, G. P., Oughton, S., Mullan, D. J., & Dmitruk, P. 1999, ApJL, 523, L93
McManus, M. D., Verniero, J., Bale, S. D., et al. 2022, ApJ, 933, 43
Mostafavi, P., Allen, R. C., McManus, M. D., et al. 2022, ApJL, 926, L38
Parashar, T. N., & Gary, S. P. 2019, ApJ, 882, 29
Parker, E. N. 1958, ApJ, 128, 664
Pugliese, F., & Dmitruk, P. 2022, ApJ, 929, 4
Robbins, D. E., Hundhausen, A. J., & Bame, S. J. 1970, JGR, 75, 1178
Scudder, J. D. 1992, ApJ, 398, 299
Stansby, D., Perrone, D., Matteini, L., Horbury, T. S., & Salem, C. S. 2019, A&A, 623, L2
Telloni, D., Antonucci, E., & Dodero, M. A. 2007, A&A, 472, 299
Tracy, P. J., Kasper, J. C., Raines, J. M., et al. 2016, PhRvL, 116, 255101
Verscharen, D., Bourouaine, S., & Chandran, B. D. G. 2013, ApJ, 773, 163
Verscharen, D., Chandran, B. D. G., Bourouaine, S., & Hollweg, J. V. 2015, ApJ, 806, 157
Wu, T. 2020, PhD Thesis, School of Earth and Space Sciences, Peking Univ.
Zhu, X., Verscharen, D., He, J., Maruca, B. A., & Owen, C. J. 2023, ApJ, 956, 66